CrossMark

Very Metal-poor Stars in the Solar Vicinity: Age Determination

Anastasiia Plotnikova[1] , Giovanni Carraro[1] , Sandro Villanova[2] , and Sergio Ortolani[1]
[1] Dipartimento di Fisica e Astronomia, Universitá di Padova, I-35122, Padova, Italy
[2] Departamento de Astronomia, Casilla 160-C, Universidad de Concepción, Concepción. Chile

Abstract

The ages of the oldest and most metal-poor stars in the Milky Way bear important information on the age of the universe and its standard model. We analyze a sample of 28 extremely metal-poor field stars in the solar vicinity culled from the literature and carefully determine their ages. To this aim, we critically make use of Gaia data to derive their distances and associated uncertainties. Particular attention has been paid to the estimate of the reddening and its effect on the derivation of stellar ages. We employed different reddenings and superimpose isochrones from different sources on the stars' color–magnitude diagram built up with different photometric systems. We highlight subtle metallicity effects when using the Johnson photometry for low-metallicity stars and finally adopt Gaia photometry. An automatic fitting method is devised to assign ages to each individual star taking into account the uncertainties in the input parameters. The mean age of the sample turns out to be 13.9 ± 0.5 Gyr using Padova isochrones, and 13.7 ± 0.4 Gyr using BASTI isochrones. We found also a group of very metal-poor stars ([Fe/H] = -2.7 to -2.0 dex) with relatively young ages, in the range 8–10 Gyr.

1. Introduction

Stars with extremely low metal abundance are of particular astrophysical and cosmological interest because they probe very early times in the evolution of the universe and its Galactic components. Through the investigation of the age and chemical composition, we can obtain important constraints on the evolution of the Milky Way, set a lower limit to the age of the universe (Bond et al. 2013; VandenBerg et al. 2014), and understand the chemical properties of the first Population III supernovae in the nascent Milky Way (Frebel & Norris 2015).

Over the years, several spectroscopic campaigns have been conducted to study the chemical composition of very metal-poor stars (Cayrel et al. 2004; Christlieb et al. 2004; Barklem et al. 2005; Schlaufman & Casey 2014; Limberg et al. 2021, etc.). The most recent investigations of the age of metal-poor stars (Bonaca et al. 2020; Carter et al. 2021) showed that they are on average old (12.0 ± 1.5 Gyr for turnoff stars). However, both groups discovered the presence of very metal-poor stars with relatively young ages of 8–10 Gyr (three stars in Bonaca et al. 2020, one star in Carter et al. 2021).

The current best estimate of the age of the universe is 13.77 ± 0.06 Gyr, based on the latest Wilkinson Microwave Anisotropy Probe derivation (Bennett et al. 2013), and it is in excellent agreement with observations of the cosmic microwave background (CMB) using the Planck satellite (Ade et al. 2014). Recent simulations (e.g., Ritter et al. 2012; Safranek-Shrader et al. 2014) suggest that the oldest Population II stars probably formed ~0.2–0.3 Gyr after the Big Bang, depending on how quickly the gas from the first (Population III) supernovae was able to cool down and condense, as well as on the relevance and impact of the Population III stellar feedback. Precise ages for the oldest and most metal-poor stars can date the onset of star formation (e.g., Bromm & Larson 2004)

following the Big Bang. Since the oldest stars must be younger than the universe, precise ages provide a strong test of the consistency between cosmological and stellar physics.

Moreover, the derived age together with high-precision spectroscopic measurements of metallicity can help us to reconstruct the age–metallicity relation (AMR)—one of the main observational constraints for any Milky Way formation and evolution model. The first AMR in the solar neighborhood was obtained by Twarog (1980) and it shows an average decrease of the metallicity with the age. Twarog (1980) concluded that the AMR can be used to estimate the star formation rate via comparison with theoretical models. That means that the AMR is an important tracer of the star formation history of galaxies. An extension of the AMR to the very metal-poor tail will help to understand the early stages of star formation in the Milky Way and in the universe.

That said, the wide distribution in metallicity in the solar neighborhood, at any given age, suggests that stars have been moving away from their birth locations over time (radial migration; Grenon 1972, 1989). The main mechanisms of radial migration are: transient spiral modes mostly at the corotation resonance (Sellwood & Binney 2002) and non-axisymmetric perturbations to the potential such as bars or galaxy interactions (Roškar et al. 2008; Quillen et al. 2009; Bird et al. 2012).

A recent intriguing finding, described in Feuillet et al. (2018), is that the youngest stars are not the most metal-rich as previously expected from pure gas enrichment processes. There are two possible reasons for such an occurrence: (1) two modes of star formation, where part of the metal-rich gas is diluted to form stars that are subsequently more metal-poor, or (2) migration of the old, metal-rich stars from the inner to the outer regions of the Galaxy. That means that nonlinear patterns in the AMR are correlated with the specific events in star formation and dynamical evolution of the Galaxy.

In this study, ages and chemical compositions of a sample of very metal-poor stars are investigated. Our main goal is to compare them with the age of the universe (13.77 ± 0.06 Gyr)
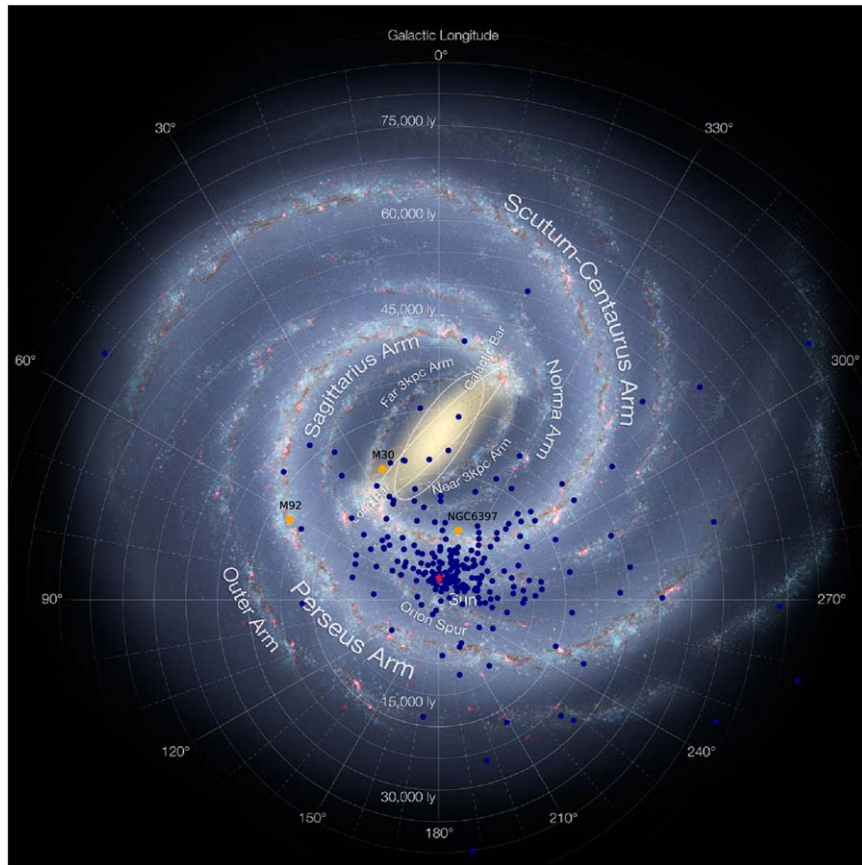
Figure 1. Location of 253 very metal-poor stars (blue) in Galactic plane. Yellow dots are metal-poor globular clusters: NGC 6397, M30, and M92. Red stars are stars: HD 84937, HD 132475, and HD 140283 (VandenBerg et al. 2014).

based on data from the CMB, baryon acoustic oscillations, and the Hubble constant (Bennett et al. 2013). We also investigate the chemical composition of these stars to retrieve information about the first Population III supernovae, the chemical composition of the nascent Milky Way, and the AMR behavior in the very metal-poor regime.

2. Data

As the main target of our research, we used metal-poor stars from the Hamburg/ESO R-process Enhanced Star (HERES) survey, spectroscopically studied by Barklem et al. (2005). Their snapshot spectra cover a wavelength range of 3760–4980 Å and have an average signal-to-noise ratio of $S/N \sim 54$ per pixel over the entire spectral range. A $2''$ slit is employed giving a minimum resolving power of $R \approx 20,000$. From the "snapshot" spectra the elemental abundances of moderate precision (absolute rms errors of order 0.25 dex, relative rms errors of order 0.15 dex) have been obtained for 22 elements: C, Mg, Al, Ca, Sc, Ti, V, Cr, Mn, Fe, Co, Ni, Zn, Sr, Y, Zr, Ba, La, Ce, Nd, Sm, and Eu.

We chose this particular data set because of its careful and detailed chemical analysis. It is indeed a unique data set from this point of view. Besides, all stars in the data set under investigation are very metal-poor and this gives us the real opportunity to study the very beginning of the formation and evolution of our Galaxy. Additionally, we want to test the cosmological age of the universe, and very metal-poor stars are the best candidates for this purpose.

The final sample of stars analyzed in Barklem et al. (2005) contains 253 stars built up with the following criteria:

1. No strong molecular carbon features in spectra
2. Metallicity cutoff: $[Fe/H] < -1.5$
3. Temperature cutoff: $T_{eff} > 4200$ K
4. No spectroscopic binaries or rotators

We complemented spectroscopic data with Gaia (G, G_{BP}, G_{RP}) and Johnson (B, V, I) photometry obtained from the Gaia archive[3] and SIMBAD catalog.[4] The distribution in the Galactic plane is shown in Figure 1. Out of these 253 stars, only 28 were turnoff (TO) stars for which we could measure good ages (see Section 8). Coordinates, photometry, interstellar absorption, distance, temperature, and chemical abundances of these 28 stars are presented in Table 1. See Sections 3 and 4 for interstellar absorption and distance determination. The main characteristics of the data set are:

1. Location in the space: Galactic halo $|b| > 20°$.
2. Most of the stars have magnitudes in the range $12 < G < 17$.
3. Distance (estimated using Gaia Data Release 3 parallaxes) in the range $0 < d < 30$ kpc.
4. Metallicity in the range $-3.8 < [Fe/H] < 1.5$ dex.
5. All stars are α-element enhanced
6. All targets are single stars. Spectroscopic binaries were already removed by Barklem et al. (2005). We checked,

---

Table 1
Parameters for the Stars Analyzed in This Study

ID	R.A. J2000	Decl. J2000	B mag	V mag	I mag	G mag	G_{BP} mag	G_{RP} mag	A_V mag	d pc	T_{eff} K	[Fe/H] dex	[C/Fe] dex
HE_0023-4825	00 25 50.31	−48 08 27.01	14.298	13.830	13.161	13.667	13.945	13.218	0.032	1164	5816	−2.06	0.31
HE_0109-3711	01 11 38.40	−36 55 17.11	16.668	16.290	15.691	16.160	16.400	15.757	0.025	3662	6156	−1.91	0.31
HE_0231-4016	02 33 44.39	−40 03 42.72	16.494	16.090	15.475	15.939	16.185	15.532	0.036	2634	5972	−2.08	1.36
HE_0340-3430	03 42 04.76	−34 20 50.10	⋯	14.783	14.189	14.657	14.910	14.238	0.031	1780	5914	−1.95	0.06
HE_0430-4404	04 31 38.10	−43 57 48.71	⋯	15.724	15.166	15.629	15.868	15.236	0.035	1569	6214	−2.07	1.44
HE_0447-4858	04 49 01.00	−48 53 36.15	16.687	16.254	15.624	16.140	16.398	15.727	0.038	3261	5995	−1.69	0.04
HE_0501-5139	05 02 48.21	−51 35 36.30	16.573	16.094	15.475	15.980	16.250	15.543	0.059	4539	5861	−2.38	0.40
HE_0519-5525	05 19 59.15	−55 22 41.81	15.570	15.034	14.284	14.862	15.171	14.374	0.066	2376	5580	−2.52	0.29
HE_0534-4615	05 35 52.94	−46 13 35.97	⋯	15.056	14.317	14.896	15.231	14.382	0.062	2266	5506	−2.01	0.13
HE_0938+0114	09 40 43.20	+01 00 29.51	⋯	⋯	⋯	10.344	10.560	9.964	0.034	180	6777	−2.51	0.65
HE_1052-2548	10 55 20.53	−26 04 48.03	13.492	13.188	12.541	13.115	13.364	12.699	0.127	675	6534	−2.29	0.51
HE_1105+0027	11 07 49.50	+00 11 38.34	16.038	15.646	15.018	15.594	15.852	15.166	0.005	3162	6132	−2.42	2.00
HE_1225-0515	12 28 12.42	−05 31 40.63	⋯	15.584	14.947	15.524	15.767	15.118	0.005	2410	6210	−1.96	0.52
HE_1330-0354	13 33 10.67	−04 10 05.80	15.248	15.000	14.380	14.937	15.169	14.537	0.082	1716	6257	−2.29	1.05
HE_2250-2132	22 53 40.48	−21 16 23.96	14.905	14.392	13.662	14.220	14.526	13.735	0.027	1780	5705	−2.22	0.41
HE_2347-1254	23 50 10.01	−12 37 50.46	13.839	13.358	12.779	13.248	13.499	12.833	0.064	783	6132	−1.83	0.27
HE_2347-1448	23 49 58.34	−14 32 15.60	15.692	15.226	14.615	15.109	15.374	14.672	0.050	3062	6162	−2.31	0.50
HE_0244-4111	02 45 57.45	−40 59 06.81	15.531	15.025	14.302	14.839	15.141	14.356	0.075	2380	5624	−2.56	0.25
HE_0441-4343	04 43 20.43	−43 38 20.51	⋯	15.559	14.835	15.388	15.695	14.904	0.047	3511	5629	−2.52	0.33
HE_0513-4557	05 15 12.21	−45 54 10.46	16.279	15.743	15.045	15.609	15.913	15.133	0.038	3602	5629	−2.79	0.39
HE_0926-0508	09 28 55.35	−05 21 40.48	12.340	12.194	11.617	12.126	12.357	11.735	0.086	457	6249	−2.78	0.62
HE_1006-2218	10 09 00.69	−22 33 30.00	⋯	13.773	13.197	13.717	13.936	13.345	0.102	928	6638	−2.69	9.99
HE_1015-0027	10 17 35.70	−00 42 24.30	15.621	15.342	14.701	15.271	15.519	14.846	0.145	1886	6315	−2.66	9.99
HE_1120-0153	11 22 43.39	−02 09 36.69	12.210	11.789	11.036	11.646	11.884	11.242	0.110	509	6191	−2.77	0.63
HE_1126-1735	11 28 51.39	−17 51 42.82	⋯	15.965	15.232	15.890	16.166	15.445	0.132	4118	5689	−2.69	0.23
HE_1413-1954	14 16 04.71	−20 08 54.09	⋯	15.235	14.593	15.171	15.418	14.745	0.225	1966	6533	−3.22	1.45
HE_2222-4156	22 25 28.65	−41 40 57.72	⋯	15.332	14.583	15.252	15.538	14.783	0.042	2773	5537	−2.73	0.42
HE_2325-0755	23 27 59.61	−07 39 13.49	14.481	13.940	13.251	14.200	14.452	13.776	0.044	1600	5665	−2.85	0.21

Table 2
Characteristics of the BaSTI and Padova Isochrones Used in This Study

Parameter	BaSTI	Padova
Age	1–15 Gyr with step 0.1 Gyr	1–20 Gyr with step 0.1 Gyr
[Fe/H]	−1.05, −1.2, −1.3, −1.4, −1.55, −1.7, −1.9, −2.2, −2.5, −3.2	−1.0 to −2.2 dex with step 0.1 dex
Heavy element mixture	[α/Fe] = +0.4	[α/Fe] = +0.0
Photometric system	UBVIJHK, Gaia DR3	UBVIJHK, Gaia DR3

however, El-Badry et al. (2021) for spatially resolved binaries. No overlap was found.

To derive age, we used two different sets of isochrones for old metal-poor populations: Padova isochrones[5] and a Bag of Stellar Tracks and Isochrones (BaSTI).[6]

We used these two sources of isochrones to check for systematics due to differences in stellar evolution models. For example, Padova isochrones do not take into account α-enhancement, while most of the studied stars are α-enhanced. BaSTI isochrones instead have a main sequence bluer than the reference globular clusters (Hidalgo et al. 2018). We can notice that for lower metallicity ([Fe/H] = −2.2), the two sets of isochrones are in a good agreement in the turnoff-point region, but BaSTI isochrones have slightly bluer main sequences and the red giant branch is more vertical. Instead, for higher metallicity ([Fe/H] = −1.2), the shift between isochrones is more evident. BaSTI isochrones are fainter and redder. The reason for this shift could be that they take into account

α-enhancement that displaces isochrones toward higher metallicity (Salaris et al. 1993). Table 2 gives a summary of the isochrones we used in this study.

In order to use Padova isochrones properly, we need to correct them for α-enhancement. To do so we used the technique proposed by Salaris et al. (1993), in which α-enhanced isochrones can be reproduced by standard isochrones if a metallicity given by the following equation is used:

$$Z = Z_0(0.638 f_\alpha + 0.362) \tag{1}$$

where $f_\alpha = \frac{Z}{Z_{Sun}} = 10^{\left[\frac{element\ abundance}{Fe}\right]}$.

The result of α-correction is shown in Figure 2. In this plot, we can see that the correction for α-enhancement increases the total metallicity on average by 0.2 dex. Moreover, the discussion in Section 7 indicates a good agreement between the stars' distribution and the isochrones, both color coded with metallicity.

3. Reddening

In this work we used two photometric systems: Gaia (G, G_{BP}, G_{RP}) and Johnson (B, V). Both of them cover the optical part of the spectrum, and thus they are quite sensitive to

---
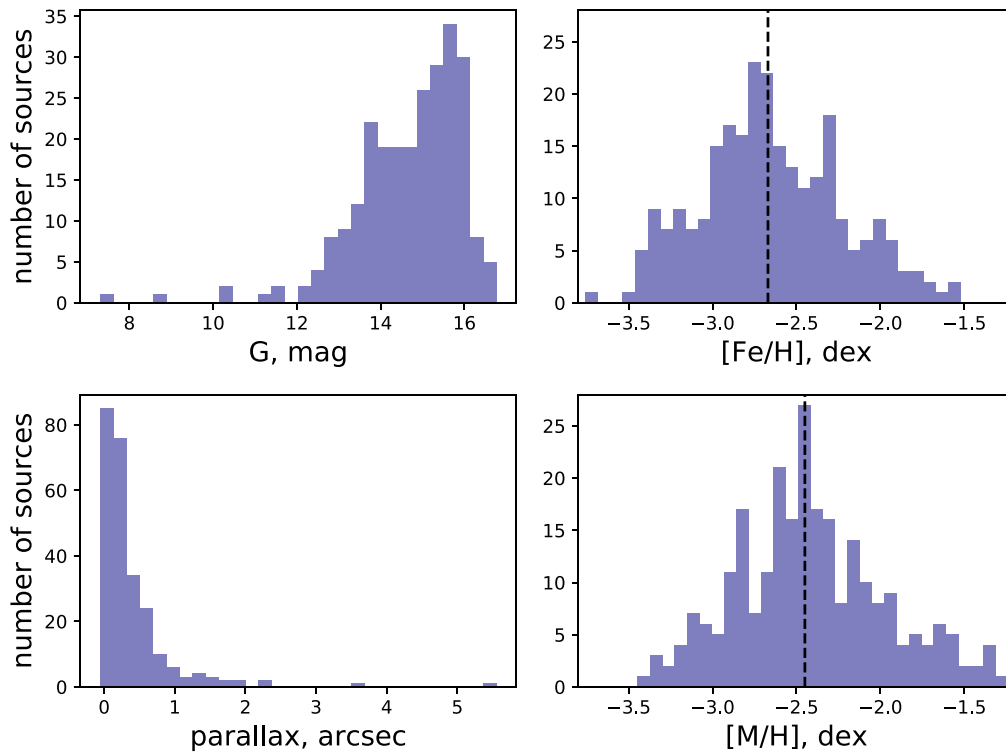
Figure 2. Distribution of very metal-poor stars in G-band magnitude (Gaia DR3; top left), in parallax (Gaia DR3; bottom left), in total metallicity (bottom right), and in [Fe/H] (top right); the vertical dashed line is the metallicity mean.

Table 3
Extinction Sources

Source	Year	Type of map	Coverage	Accuracy
Schlegel et al.	1998	2D	all sky	16%
Schlafly & Finkbeiner	2011	2D	all sky	50 mmag
Queiroz et al. (StarHorse)	2020	3D	$\|z_{Gal}\| < 1$ kpc, $R_{Gal} \lesssim 20$ kpc	50–200 mmag
Green et al.	2018	3D	$\delta \gtrsim -30°$, $d^a \lesssim 60$ kpc	10–100 mmag
Lallement et al.	2018	3D	$D^b \leqslant 4000$ pc, $\|z_{Gal}\| \leqslant 600$ pc	10–150 mmag
Montalto et al.	2021	method	$d \lesssim 2.5$ kpc	

Notes.
[a] Distance from the Sun
[b] Distance from the Sun in the Galactic disk

reddening. Therefore, correction for reddening is a critical step in our analysis. Our targets are located in the Galactic halo ($|b| > 20°$). The Galactic halo is poor in gas and dust and, as a consequence, it does not exhibit significant extinction. But even small reddening corrections might cause big uncertainties in age determination; that is why we used the five different sources of extinction values listed in Table 3 to get the best estimate for that effect.

Schlegel et al. (1998) is a full-sky 100 μm 2D map that is a reprocessed composite of the COBE/DIRBE and IRAS/ISSA maps, where the zodiacal foreground and confirmed point sources are removed. The uncertainty of the map is around 16%.

Schlafly & Finkbeiner (2011) presented a full-sky 2D dust reddening map measured as the difference between the measured and predicted colors of a star, as derived from stellar parameters from the Sloan Extension for Galactic Understanding and Exploration Stellar Parameter Pipeline. They achieve uncertainties of 56, 34, 25, and 29 mmag in the colors u–g, g–r, r–i, and i–z, per star, though the uncertainty varies depending on the stellar type and the magnitude of the star.

StarHorse extinction values are computed by the Bayesian isochrone-fitting technique with stellar parameters (T_{eff}, log g, [M/H]) from spectroscopy, photometric magnitude (m_λ), parallax from Gaia DR2, and PARSEC isochrones. The extinction uncertainties are ~70 mmag when all photometric information is available, and ~170 mmag if optical photometry is missing. For our data set, the most common value of the uncertainty is ~200 mmag (see also Section 4.4). Queiroz et al. (2020) provide a coverage of the disk close to the Galactic midplane ($|z_{Gal}| < 1$ kpc) from the Galactic center out to $R_{Gal} \sim 20$ kpc.

Green et al. (2018) produced a new 3D map of interstellar dust reddening, covering three quarters of the sky (declinations of $\delta \gtrsim -30°$) out to a distance of several kiloparsecs. The map is based on high-quality stellar photometry of 800 million stars from PanSTARRS 1 and 2MASS. They divide the sky into sightlines containing a few hundred stars each, and then infer stellar distances and types, along with the line-of-sight dust distribution. For our data set, the mean uncertainty of this map is about 20 mmag.
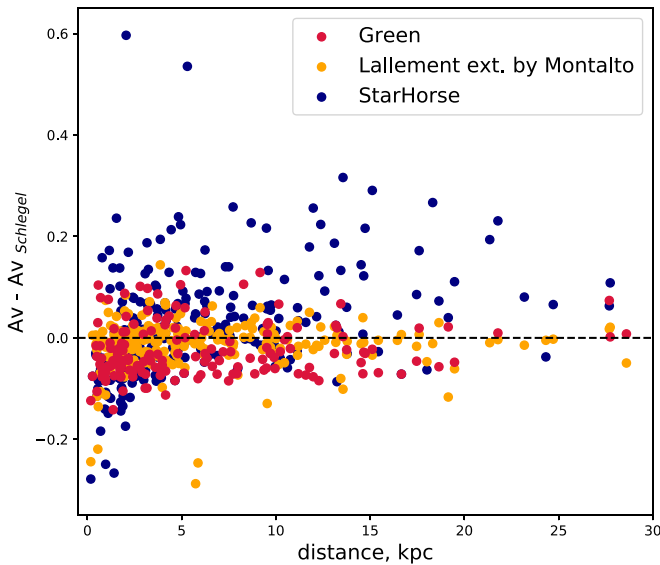
Figure 3. Comparison of reddening from Green et al. (2018), Lallement et al. (2018) extended by Montalto et al. (2021), and StarHorse, with reddening from Schlegel et al. (1998) as a function of distance.

Lallement et al. (2018) selected low-reddening Sloan Digital Sky Survey APOGEE-DR14 red giants to obtain an empirical effective temperature- and metallicity-dependent photometric calibration in the Gaia G and 2MASS K_s bands. This calibration has been combined with Gaia G-band empirical extinction coefficients recently published, G, J, and K_s photometry, and APOGEE atmospheric parameters to derive the extinction of a large fraction of the survey targets. Distances were estimated independently using isochrones and the magnitude-independent extinction $K_{J−Ks}$. This new data set has been merged with the one used for the earlier version of the dust map. A new Bayesian inversion of distance–extinction pairs has been performed to produce an updated 3D map that covers $4000 \times 4000 \times 600$ pc^3 around the Sun. The uncertainty of this map for our data set varies from 10 to 150 mmag.

To extend the Lallement et al. (2018) map to larger distances, we applied the method illustrated in Montalto et al. (2021). They suggested to use the dust distribution model of the Milky Way to calculate the amount of dust between the edge of the Lallement et al. (2018) map and the real position of the object. It can be applied if there are no specific dust and gas structures, which is almost true for the halo where all stars under consideration are located. In Montalto et al. (2021), the extension method was applied to stars not farther than 2.5 kpc and showed good agreement with the photometric parameters.

To get the best extinction estimate for our stars, we studied all sources of reddening corrections listed in Table 3. Since the range in distances for our stars is from 0.2 to 30 kpc (see Section 4), it is more precise to use a 3D map instead of 2D, which additionally has lower accuracy. In Figure 3 we can see that the Lallement et al. (2018) map, extended by Montalto et al. (2021), and the map of Green et al. (2018) show good agreement with each other and with the Schlegel et al. (1998) 2D map for far distances, for stars closer to the Sun, the Schlegel et al. (1998) map reddening is greater. StarHorse reddening instead shows a larger dispersion in all distance ranges and on average larger reddening values compared to the Schlegel et al. (1998) map. Therefore, by comparing the three latest 3D maps, we chose to use only the Lallement et al. (2018)

extended by Montalto et al. (2021) and that of Green et al. (2018). Both these maps have weak points. For example, the Green et al. (2018) map covers only three quarters of the sky. Lallement et al. (2018) does not have high accuracy in all directions. That is why our solution was to combine the two reddening maps together by choosing for each star the best extinction estimate from Lallement et al. (2018) extended by Montalto et al. (2021) or from Green et al. (2018). The resulting reddening correction is shown in Figure 4. We can see that the combined map shows the smallest dispersions in the color–magnitude diagram (CMD).

4. Distance Determination

Stellar distances constitute a fundamental quantity in astrophysics. In fact, we need distances to compute absolute magnitudes for each metal-poor star in our data set. Distance is one of the crucial parameters that affect the obtained results. For this purpose we used four different techniques: Gaia DR3 parallaxes (Gaia Collaboration et al. 2022), Gaia EDR3 parallaxes (Gaia Collaboration 2021) corrected by Lindegren et al. (2021), the distances derived by Bailer-Jones et al. (2021), and Queiroz et al. (2020; StarHorse).

4.1. Gaia Data Release 3 (Gaia DR3) Parallaxes

The first main technique is parallax distance. Today we have very accurate trigonometric parallaxes (see Table 4 for uncertainties) obtained by the Gaia satellite for about 1.47 billion stars (Gaia Collaboration et al. 2022). From these trigonometric parallaxes, distance can be obtained through the following equation:

$$d = \frac{1}{\pi} \tag{2}$$

where d is the distance to the object in parsecs and π is its trigonometric parallax in arcseconds. The problem with this distance determination is that, due to the structure of this equation, uncertainties on the distance are not symmetric around the mean value, especially for a large uncertainty on the parallax. That is why errors for each source must be computed separately for the higher and lower edges of the distance:

$$d_{\text{low}} = \frac{1}{\pi + \Delta\pi} \tag{3}$$

$$d_{\text{high}} = \frac{1}{\pi - \Delta\pi}. \tag{4}$$

Uncertainties of Gaia DR 3 astrometry as given by the Gaia Collaboration are shown in Table 4.

4.2. Corrections for Gaia EDR3 Parallaxes: Lindegren et al. (2021)

Parallaxes measured by the Gaia Collaboration (2021) can have some biases that have been measured by Lindegren et al. (2021). Lindegren et al. (2021) found that parallaxes that correspond to quasars (distant objects whose parallaxes should be distributed around zero) have a systematic offset from the expected distribution around zero by a few tens of microarcseconds. Starting from the quasars bias for faint sources, they extended the map of the correction to lower magnitudes using physical pairs (binaries) and Large Magellanic Cloud sources. The parallax bias is found to depend in a nontrivial way on (at
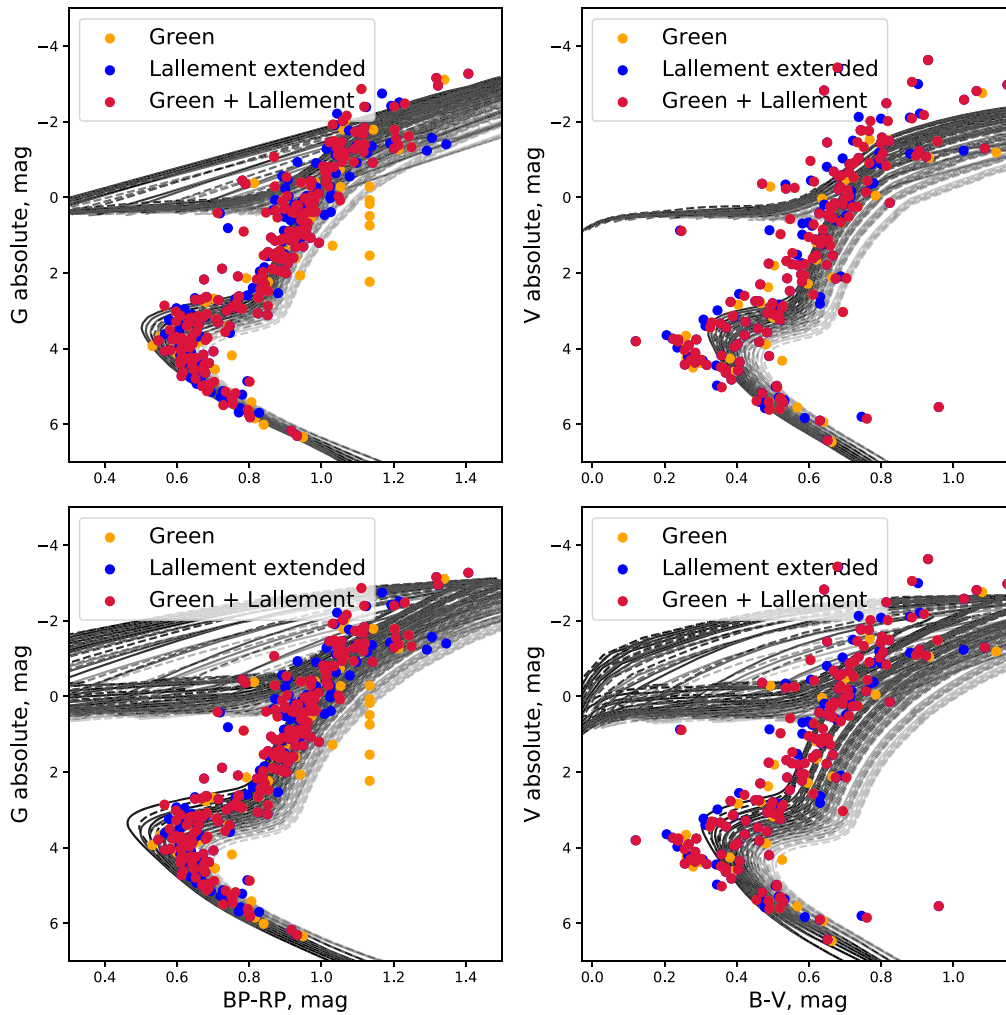
Figure 4. CMD in Gaia (first column) and Johnson (second column) photometry corrected using Lallement et al. (2018) map extended by Montalto et al. (2021), Green et al. (2018), and the best correction value from one of the two (Green+Lallement). First row: Padova isochrones ([Fe/H]: -1.0 to -2.2 dex; age: 10–15 Gyr). Second row: BaSTI isochrones ([Fe/H]: -1.0 to -3.2 dex; age: 10–15 Gyr).

Table 4
Uncertainties of Gaia DR 3 Astrometry from Gaia Collaboration (2021)

| Data product	Typical uncertainty			
	$G < 15$	$G = 17$	$G = 20$	$G = 21$
Five-parameter astrometry				
Position, mas	0.01–0.02	0.05	0.4	1
Parallax, mas	0.02–0.03	0.07	0.5	1.3
Six-parameter astrometry				
Position, mas	0.02–0.03	0.08	0.4	1
Parallax, mas	0.02–0.04	0.1	0.5	1.4

least) the magnitude, color, and ecliptic latitude of the source. Different dependencies apply to the five- and six-parameter solutions in Gaia EDR3. While it is not possible to derive a definitive recipe for the parallax correction, they give tentative expressions to be used at the researcher's discretion and point out some possible paths toward future improvements. We applied the Lindegren et al. (2021) correction for downloaded Gaia EDR3 parallaxes and then computed the distance and its lower and upper limit through Equations (2), (4), (3). The results are shown in Figure 5, second row.

4.3. Corrections for Gaia EDR3 Parallaxes: Bailer-Jones et al. (2021)

Despite Gaia EDR3's high precision, the majority of stars observed by Gaia are distant or faint so their parallax uncertainties are large, and this prevents the direct inversion of parallax for obtaining distance. That is why Bailer-Jones et al. (2021) used a probabilistic approach to estimate stellar distances that use a prior construction from a three-dimensional model of our Galaxy. This model includes interstellar extinction and Gaia's variable magnitude limit. They obtain two types of distances. The first, geometric, uses the parallax together with a direction-dependent prior on distance. The second, photogeometric, additionally uses the color and apparent magnitude of a star, by exploiting the fact that stars of a given color have a restricted range of probable absolute magnitudes (plus extinction). Tests on simulated data and external validations show that the photogeometric estimates generally have higher accuracy and precision for stars with poor parallaxes.
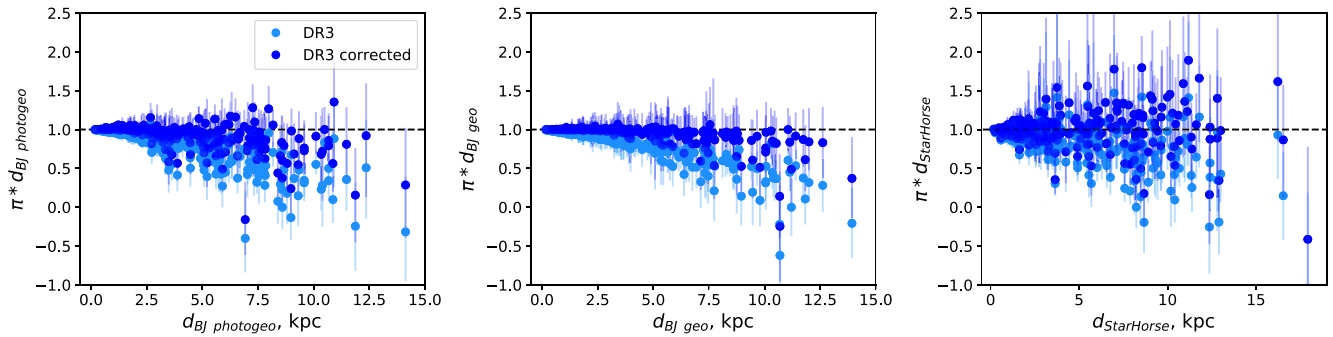
4.4. StarHorse Distances

An additional source of distances is the APOGEE DR16 `StarHorse` catalog where Queiroz et al. (2020) combined
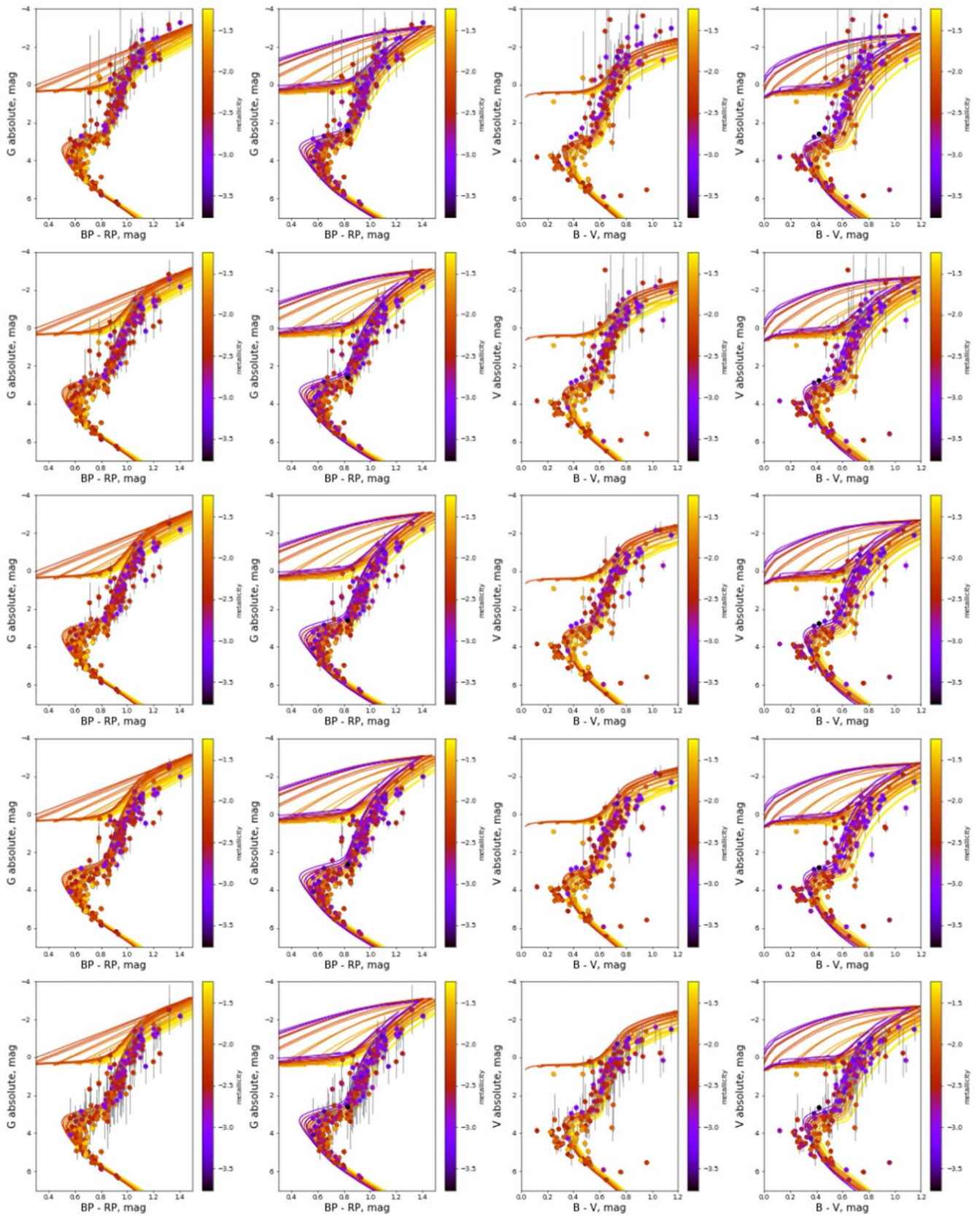
Figure 5. Gaia (first two columns) and Johnson (last two columns) photometry color coded according to the corrected metallicity for Padova isochrones (first and third columns) and to the observed metallicity for BaSTI isochrones (second and fourth columns). Distances are computed by Gaia DR3 parallaxes (first row), Gaia EDR3 parallaxes corrected by Lindegren et al. (2021; second row), Bailer-Jones et al. (2021; geo, third row and photogeo, fourth row), and computed by Queiroz et al. (2020; StarHorse, fifth row). Isochrones are color coded according to metallicity ([Fe/H]: −1.0 to −2.2 dex, age: 10–15 Gyr (Padova); [Fe/H]: −1.0 to −3.2 dex, age: 10–15 Gyr (BaSTI)).

Figure 6. Comparison of parallax from Gaia DR3 (light blue) and corrected Gaia EDR3 by Lindegren et al. (2021; blue) with geometric (left) and photogeometric (middle) distance from Bailer-Jones et al. (2021) and with the `StarHorse` distance from Queiroz et al. (2020; right). The vertical axis shows the Gaia DR3 parallax and corrected parallax multiplied by the geometric distance: values under 1 correspond to the parallax distance being larger than the value of Bailer-Jones et al. (2021) or `StarHorse` distance and vice versa. The vertical error bars take into account the statistical uncertainties both on the parallax and the distance, but the horizontal error bars for the distance are not displayed.

spectroscopic (APOGEE-2 survey Data Release 16) and photometric (IR: 2MASS, AllWISE; optical: PanSTARRS 1) data as well as parallaxes (Gaia Data Release 2). They used the Bayesian isochrone-fitting code `StarHorse` to obtain distances and extinction for 388,815 APOGEE stars. All stars studied in this work are included. The typical distance uncertainties are ∼6% for APOGEE giants and ∼2% for APOGEE dwarfs. `StarHorse` uncertainties vary with the input spectroscopic catalog, available photometry, and parallax uncertainties. Data are available at https://data.aip.de/projects/aqueiroz2020.html.

4.5. Distance Choice

The comparison of distances from Bailer-Jones et al. (2021) and parallaxes from Gaia DR3 and corrected by Lindegren et al. (2021) are shown in Figure 6 (left, middle panels). The vertical axis shows the Gaia DR3 parallax and corrected parallax multiplied by the geometric (Figure 6, left panel) and photogeometric (Figure 6, middle panel) distance: values under 1 correspond to the parallax distance larger than the value of Bailer-Jones et al. (2021) distance and vice versa. The vertical error bars take into account the statistical uncertainties both on the parallax and on the distance, but the horizontal error bars for the distance are not displayed. We can see that for close objects (<3 kpc) parallaxes corrected by Lindegren et al. (2021) are in good agreement with Bailer-Jones et al. (2021) geometric and photogeometric distances. Beyond 3 kpc, the corrected parallaxes give larger distances than the geometric and the photogeometric ones. In general, Gaia DR3 parallaxes yield larger distances in all ranges of distances. Some of the stars having negative parallaxes but positive distances can be derived from Bailer-Jones et al. (2021).

From Figure 6 (right panel) we can notice that `StarHorse` distances and distances from parallax corrected by Lindegren et al. (2021) are in a good agreement. By contrast, direct distances from Gaia EDR3 parallaxes show larger values. However, to consider the best estimate of distances for our data set, a deeper investigation should be done using a CMD and the isochrone-fitting technique. In Figure 5, stars are corrected for reddening with combined Green et al. (2018) + Lallement et al. (2018) extended by Montalto et al. (2021) map and are color coded with the corrected metallicity for Padova isochrones and the observed metallicity for BaSTI isochrones. The metallicity range for Padova isochrones is −1.3 to −2.2 dex and for BaSTI isochrones is −1.3 to −3.2 dex. For each metallicity, 10 and

15 Gyr isochrones are plotted, color coded with metallicity. Comparing different methods for distance determination, we can highlight the following discrepancies, depending on the distance technique we use:

1. Some stars are located in low-probability regions, such as above the main sequence and below the subgiant branch, or on the red side of the red giant branch (Gaia DR3 parallaxes, Lindegren, Bailer-Jones, `StarHorse`).
2. There is a non-negligible shift in the position of red giant branch and turnoff stars in comparison with the isochrones of the same metallicity (Lindegren, Bailer-Jones, `StarHorse`).
3. Different shapes of the observed red giant branch are visible compared with the shape of isochrone red giant branch (Lindegren, Bailer-Jones, `StarHorse`).

According to the above criteria, we can conclude that Gaia parallaxes show the best fit to the data. In this case, we can see also that fewer targets lie in the low-probability region. Moreover, all stars with metallicities lower than the lower limit for the isochrone metallicity range lie above the red giant branch where the estimated position of these stars should be. The Lindegren et al. correction and `StarHorse` distances move low-metallicity stars in the red giant branch to the position of isochrones with higher metallicity and break the shape of the red giant branch. The Bailer-Jones et al. distances additionally shift more stars to the low-probability region, which reduces the quality of the data set. All these tests show that the best distance estimate estimator for our purposes is the distance obtained by directly inverting Gaia parallaxes.

A possible explanation for the lower accuracy we obtained by applying the Lindegren et al. (2021) correction is that they are based on faint sources and, as a consequence, they are less accurate for brighter magnitudes, as our targets have. Bailer-Jones et al. also used the Lindegren et al. correction as an input. Because of this, their corrections are affected by the same bias. `StarHorse` distances are less precise instead because Queiroz et al. (2020) used Gaia DR 2 parallaxes as prior for the distance calculation, which have a lower accuracy compared with new Gaia DR3 parallaxes.

5. Derivation of the Absolute Magnitude

To compare isochrones with observational data, we need to convert observed G photometry to its absolute magnitude. To

	B	V	I	G	G_{BP}	G_{RP}
A_λ/A_V	1.326	1.000	0.599	0.861	1.061	0.648

do this we need to apply the distance modulus and reddening correction using:

$$M_\lambda = m_\lambda + 5 - 5 \cdot \log(d) - A_\lambda$$

where d is the distance to the star in parsecs and $A_G = A_V \times$ coef (for coef, see Table 5). These transformations assume the standard reddening law $A_V = R_V \times E(B-V)$ with $R_V = 3.1$, since all our targets are far from the Galactic plane or the Galactic bulge, where R_V can assume different values.

6. Differences in CMDs for Different Photometric Systems

A closer look at the data reveals additional peculiarities. Figure 5 shows that some turnoff stars in the Johnson photometry (the two columns on the right) are blueshifted with respect to the isochrones, and also if compared with their position in the Gaia photometry (the two columns on the left). In order to investigate more deeply this behavior, we performed further tests.

First of all, we color coded our data according to Galactic latitude (Figure 7, top row). The bottom-left panel of this figure shows the position of the targets on the V versus $B-V$ CMD. It is clear that all the stars with the larger turnoff shift are located at positive Galactic latitude, while all the other stars have negative Galactic latitudes. The difference in position might indicate a difference in reddening, but since our data set is corrected for it, only a particularly improbable kind of extinction could explain this behavior. By contrast, Figure 7 (bottom-right panel) shows the V versus $V-I$ CMD, where we do not see such an affect. This means that the shift is entirely due to the B filter.

6.1. Chemical Analysis

One of the reasons why stars with the same temperature (as inferred from the $G_{BP}-G_{RP}$ and $V-I$ colors) and luminosity (as inferred from G and V magnitudes) differ in just one of the filters is that this filter contains strong molecular bands and that the elements responsible for these bands (usually C, N, and O) vary their abundances from one star to the other. Also, chemical abundance variations of C, N, O, Ne, Mg, Si, S, Ca, and Fe affect the opacity of the star and change the continuum emission in that part of the spectrum (Salaris et al. 1993). To check these effects, we downloaded from the ESO database[7] flux-calibrated UVES spectra for pairs of stars with the same T_{eff} and similar reddening ($\Delta A_V < 0.02$ mag) but different dereddened $B-V$ colors. In Figure 8, we can see that when the distance between shifted (yellow) and nonshifted (blue) stars increases, the continuum of the shifted stars also increases. It happens specifically in the range of the B filter. To check the dependence between the shift and chemical composition, we color coded CMDs with abundances of C (the only element responsible for the molecular bands we have) and Fe. From Figure 9, we can see that shifted stars are enhanced in C and more metal-poor on average. Since we see no presence of strong molecular bands in the spectra, we conclude it is the

change in the opacity of the atmospheres of the stars due to the different C and Fe content that is the cause of the shift in the $B-V$ color. Specifically, a higher [C/Fe] abundance and a lower [Fe/H] content increase the flux in the B filter.

For this reason, Johnson photometry cannot be properly used for age determination for very metal-poor stars. Gaia filters are wider and so less affected by this phenomenon, and it is the only photometry we will use for the age determination.

7. Age Determination Method

To derive age, we developed an automatic technique based on isochrone fitting. First, we filtered our data with the following criteria:

1. Distance > 0
2. Distance error $< 20\%$
3. Metallicity range: -2.3 to -1 dex for Padova isochrones; -3.3 to -1 dex for BaSTI isochrones
4. Absolute magnitude is in turnoff-point region: $2.4 < G < 4.7$ mag

The first two criteria exclude stars with bad astrometric measurements. The third cutoff is based on the metallicity range covered by the isochrone data sets. We should note that for different isochrones, the cutoff is different. And the fourth cutoff leaves only stars from the turnoff-point region—the part of the CMD most sensitive to age. The algorithm takes a set of isochrones matching the metallicity of the target and searches for the closest. Each isochrone is define by a set of X,Y points in the 2D space of the CMD. The distance used to choose the closest isochrone is the shortest between the perpendicular to one of the segments defined by two consecutive X,Y points, and the distance to the closest point of the isochrone. The age of the closest isochrone is then considered as a first guess of age of the star if the distance is less than 10^{-4} mag (the maximum distance between isochrones with an age step of 100 Myr). Otherwise, age cannot be derived, since the star is too far from all isochrones.

As a second step, we consider the mean parallax, reddening, metallicity, and photometry of each target and the related errors. Assuming a Gaussian distribution, we randomly distributed 10,000 points in the parameter space and applied the age determination technique to each of them. The result is an age histogram that is fitted with a Gaussian function. We consider its mean as the age of the star and σ as its uncertainty.

In Figure 10 we can see an illustration of the age determination for Padova and BaSTI isochrones. Isochrones have an upper limit of 20 Gyr for Padova, and from 15.4 to 19.2 Gyr (depending on metallicities) for BaSTI. Because of this, all stars redder than the oldest isochrone are considered to have the age of this isochrone. Therefore, we get some saturation in the bin corresponding to the oldest isochrone. We cut saturated bins as not representative. We derive age in three different combinations of photometric filters: G versus $G_{BP} - G_{RP}$, G versus $G_{BP} - G$, and G versus $G - G_{RP}$.

To get the best age sample, we applied the following criteria:

1. Age derived in all three filter combinations: G versus $G_{BP} - G_{RP}$, G versus $G_{BP} - G$, and G versus $G - G_{RP}$
2. Derived age is not closer to the oldest isochrone less than 1σ

In this way, we reduced the targets for which we can derive good ages to 28.

---

[7] http://archive.eso.org/scienceportal/home
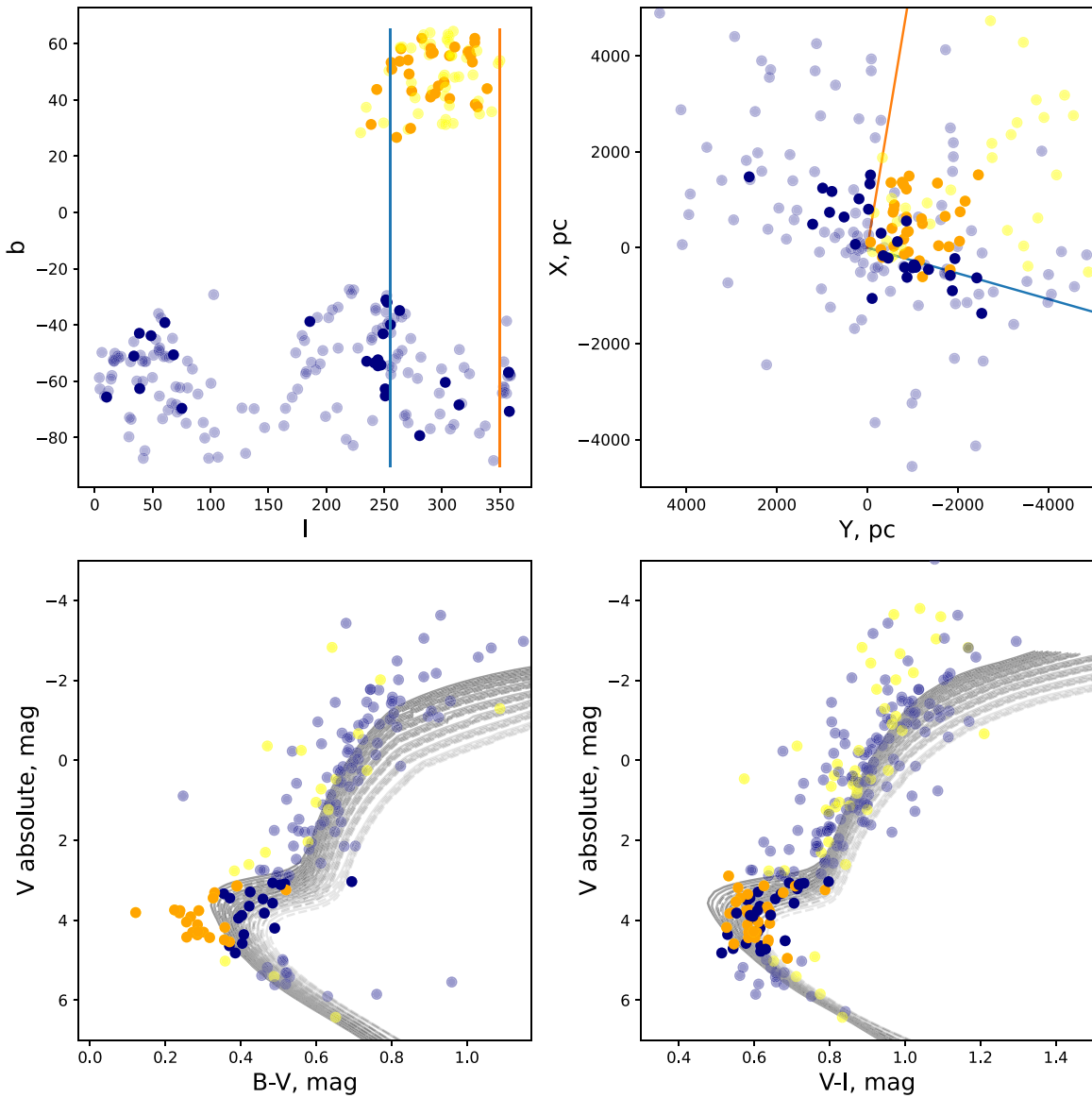
Figure 7. Top: position of our targets on the sky (left, Galactic coordinates) and in the Galactic plane (right), color coded with Galactic latitude ($b > 0$: yellow, $b < 0$: blue). Bottom: CMD in V versus $B-V$ (left) and V versus $V-I$ (right) filters;, yellow points are non-turnoff stars with $b > 0$, orange points are turnoff stars with $b > 0$, light blue points are non-turnoff stars with $b < 0$, and dark blue points are turnoff stars with $b < 0$. Padova isochrones are added as a reference ([Fe/H]: -1.0 to -2.2 dex, age: 10–15 Gyr).
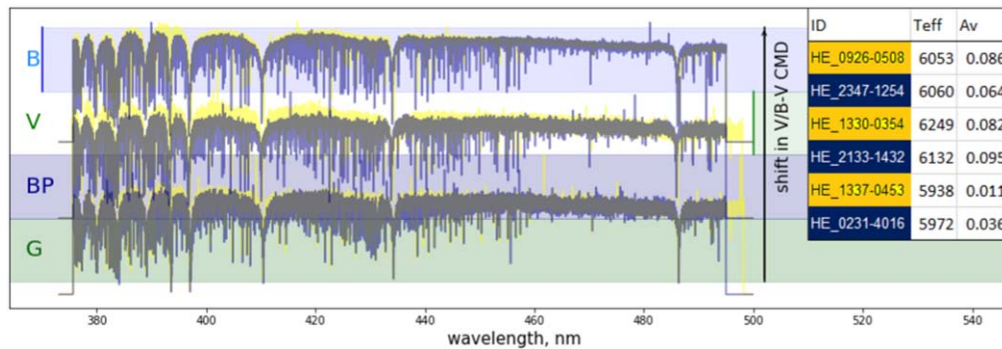

Figure 8. Comparison of the spectra for bluer and redder stars in the (V versus $B-V$) CMD. Gaia and Johnson photometric filters ranges are plotted with color: B—light blue, V—light green, BP—blue, and G—green.
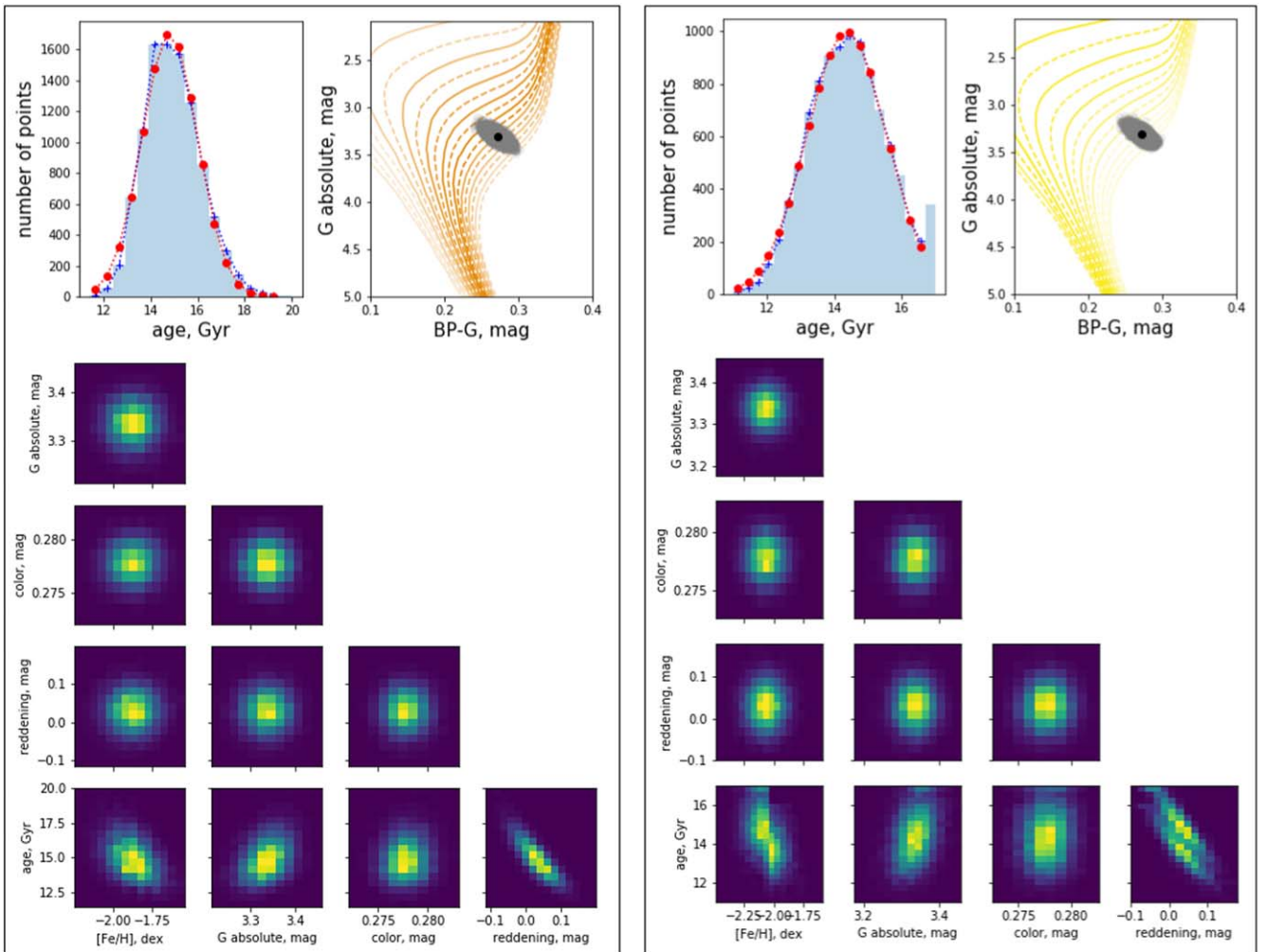
8. Results

8.1. Age

The derived ages for 28 selected stars are reported in Table 6. The distribution of the distance nd metallicity is reported in Figure 11. Out of 28, we have only 17 stars for which age is derived from both isochrone sets, and for 11 stars age was derived only from the BaSTI isochrone set due to its lower limit in metallicity. In Figure 12, on the left, we can see the dispersion of the age, where the vertical dotted line shows
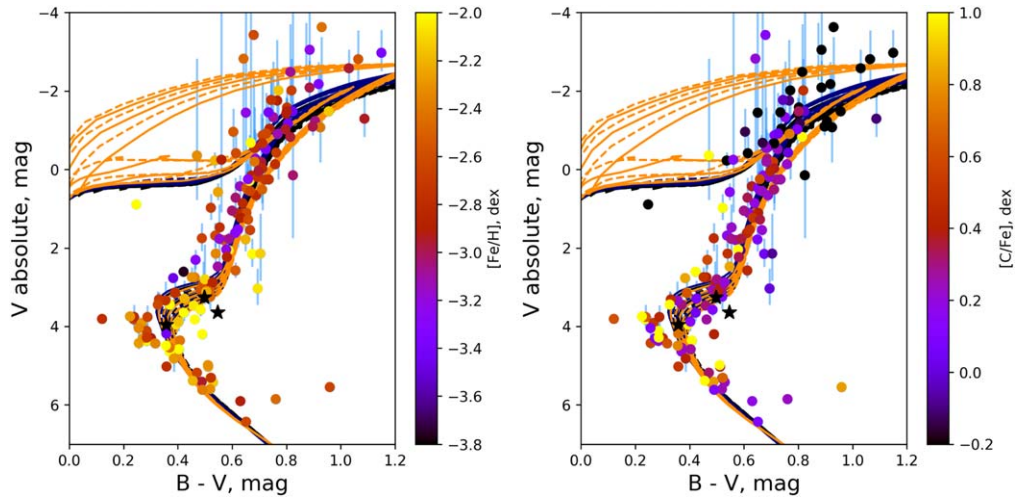
Figure 9. Johnson photometry color coded with [Fe/H] (left panel) and [C/Fe] (right panel). Distance computed by means of Gaia DR3 parallaxes. Black stars are stars: HD 84937, HD 132475, and HD 140283 (VandenBerg et al. 2014). Padova (blue) and BaSTI (orange) isochrones with [Fe/H] = −2.2 dex and ages 10–15 Gyr are added as a reference.

Figure 10. Resulting plot of age determination from Padova (left panel) and BaSTI (right panel) isochrones for star HE 0023−4825 in diagrams of G versus $G_{BP} − G$. Gray dots in the CMD are randomly selected input parameters. The black dot shows the original stellar parameters.

the age of the universe, 13.77 Gyr (Bennett et al. 2013). The right side of Figure 12 shows that, on average, the Padova isochrones show older ages, but the systematic difference is much less than 1 Gyr.

We also compared ages derived with different filter combinations: G versus $G_{BP} − G$, G versus $G − G_{RP}$, G versus $G_{BP} − G_{RP}$. The result is reported in Figure 13, where we can notice that the peak of all distributions is compatible with zero

Table 6
Ages of Metal-poor Stars

ID	[Fe/H] dex	\multicolumn{6}{Age from Padova isochrones, Gyr}						\multicolumn{6}{Age from BaSTI isochrones, Gyr}						\multicolumn{3}{Average, Gyr}		
		G versus $G_{BP} - G$		G versus $G - G_{RP}$		G versus $G_{BP} - G_{RP}$		G versus $G_{BP} - G$		G versus $G - G_{RP}$		G versus $G_{BP} - G_{RP}$		Padova	BaSTI	Padova+BaSTI
		Age	Error	Age	Error	Age	Error	Age	Error	Age	Error	Age	Error	Age	Age	Age
HE 0023-4825	−2.06	14.8	±1.2	14.9	±1.1	14.9	±1.1	14.4	±1.2	14.4	±1.2	14.4	±1.2	14.9	14.4	14.6
HE 0109-3711	−1.91	11.8	±2.3	11.9	±2.4	11.8	±2.3	11.6	±2.7	11.8	±2.7	11.7	±2.7	11.8	11.7	11.8
HE 0231-4016	−2.08	13.3	±1.3	13.3	±1.2	13.3	±1.3	15.4	±1.3	15.4	±1.2	15.4	±1.2	13.3	15.4	14.4
HE 0340-3430	−1.95	13.6	±0.9	13.6	±0.9	13.6	±0.9	12.9	±0.9	13.1	±0.9	13.1	±0.9	13.6	13.0	13.3
HE 0430-4404	−2.07	7.7	±3.0	6.6	±2.7	7.0	±2.8	13.8	±2.8	12.7	±2.5	13.2	±2.6	7.1	13.2	10.1
HE 0447-4858	−1.69	14.0	±2.1	13.4	±1.7	13.6	±1.9	13.1	±2.1	12.7	±1.9	12.9	±2.0	13.7	12.9	13.3
HE 0501-5139	−2.38	9.0	±2.3	9.0	±2.3	9.0	±2.3	8.9	±2.4	8.9	±2.4	8.9	±2.4	9.0	8.9	8.9
HE 0519-5525	−2.52	13.3	±1.8	13.6	±1.8	13.5	±1.8	13.3	±1.6	13.6	±1.6	13.5	±1.6	13.5	13.4	13.5
HE 0534-4615	−2.01	16.0	±2.9	16.0	±2.9	16.0	±2.9	13.8	±2.3	13.8	±2.2	13.9	±2.2	16.0	13.8	14.9
HE 0938+0114	−2.51	12.4	±1.9	13.8	±1.8	13.2	±1.8	13.8	±1.7	14.6	±1.0	14.3	±1.2	13.1	14.2	13.7
HE 1052-2548	−2.29	15.3	±0.7	16.1	±0.6	15.8	±0.6	15.2	±0.5	16.0	±0.4	15.7	±0.4	15.7	15.7	15.7
HE 1105+0027	−2.42	11.2	±2.1	11.4	±2.2	11.3	±2.1	12.8	±2.4	12.9	±2.4	12.8	±2.4	11.3	12.8	12.1
HE 1225-0515	−1.96	14.6	±1.6	14.6	±1.6	14.6	±1.6	14.7	±1.8	14.6	±1.6	14.7	±1.8	14.6	14.7	14.6
HE 1330-0354	−2.29	12.3	±0.9	13.3	±0.8	12.9	±0.8	13.7	±0.9	14.6	±0.8	14.2	±0.8	12.8	14.2	13.5
HE 2250-2132	−2.22	13.2	±1.2	13.6	±1.3	13.4	±1.3	12.8	±1.1	13.2	±1.3	13.0	±1.2	13.4	13.0	13.2
HE 2347-1254	−1.83	14.6	±1.7	14.6	±1.5	14.6	±1.6	14.5	±1.6	14.6	±1.4	14.4	±1.4	14.6	14.5	14.6
HE 2347-1448	−2.31	8.7	±1.8	8.8	±1.8	8.8	±1.8	8.4	±1.8	8.5	±1.9	8.5	±1.9	8.8	8.5	8.6
HE 0244-4111	−2.56	⋯	⋯	⋯	⋯	⋯	⋯	12.6	±1.3	13.0	±1.3	12.7	±1.3	⋯	12.8	⋯
HE 0441-4343	−2.52	⋯	⋯	⋯	⋯	⋯	⋯	10.3	±1.9	10.5	±1.9	10.4	±1.9	⋯	10.4	⋯
HE 0513-4557	−2.79	⋯	⋯	⋯	⋯	⋯	⋯	12.5	±2.5	12.4	±2.5	12.4	±2.5	⋯	12.4	⋯
HE 0926-0508	−2.78	⋯	⋯	⋯	⋯	⋯	⋯	14.6	±0.8	14.9	±0.6	14.8	±0.7	⋯	14.8	⋯
HE 1006-2218	−2.69	⋯	⋯	⋯	⋯	⋯	⋯	12.7	±1.1	13.1	±0.8	12.9	±0.9	⋯	12.9	⋯
HE 1015-0027	−2.66	⋯	⋯	⋯	⋯	⋯	⋯	14.9	±1.3	15.6	±1.0	15.1	±1.0	⋯	15.2	⋯
HE 1120-0153	−2.77	⋯	⋯	⋯	⋯	⋯	⋯	10.7	±0.7	11.0	±0.6	10.8	±0.6	⋯	10.8	⋯
HE 1126-1735	−2.69	⋯	⋯	⋯	⋯	⋯	⋯	9.4	±2.6	9.5	±2.6	9.4	±2.6	⋯	9.4	⋯
HE 1413-1954	−3.22	⋯	⋯	⋯	⋯	⋯	⋯	13.1	±0.9	15.3	±1.5	14.2	±1.2	⋯	14.2	⋯
HE 2222-4156	−2.73	⋯	⋯	⋯	⋯	⋯	⋯	13.3	±2.4	13.7	±2.4	13.5	±2.4	⋯	13.5	⋯
HE 2325-0755	−2.85	⋯	⋯	⋯	⋯	⋯	⋯	13.3	±1.2	13.6	±1.2	13.6	±1.2	⋯	13.5	⋯
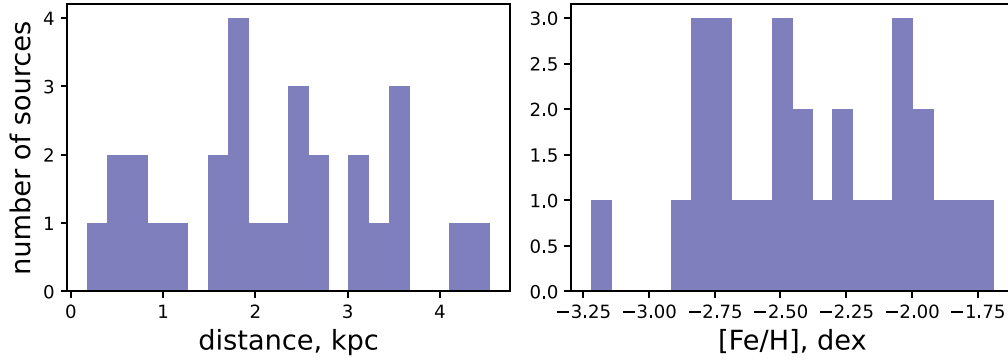
Figure 11. Distribution of the distance and metallicity for the 28 stars with derived ages.
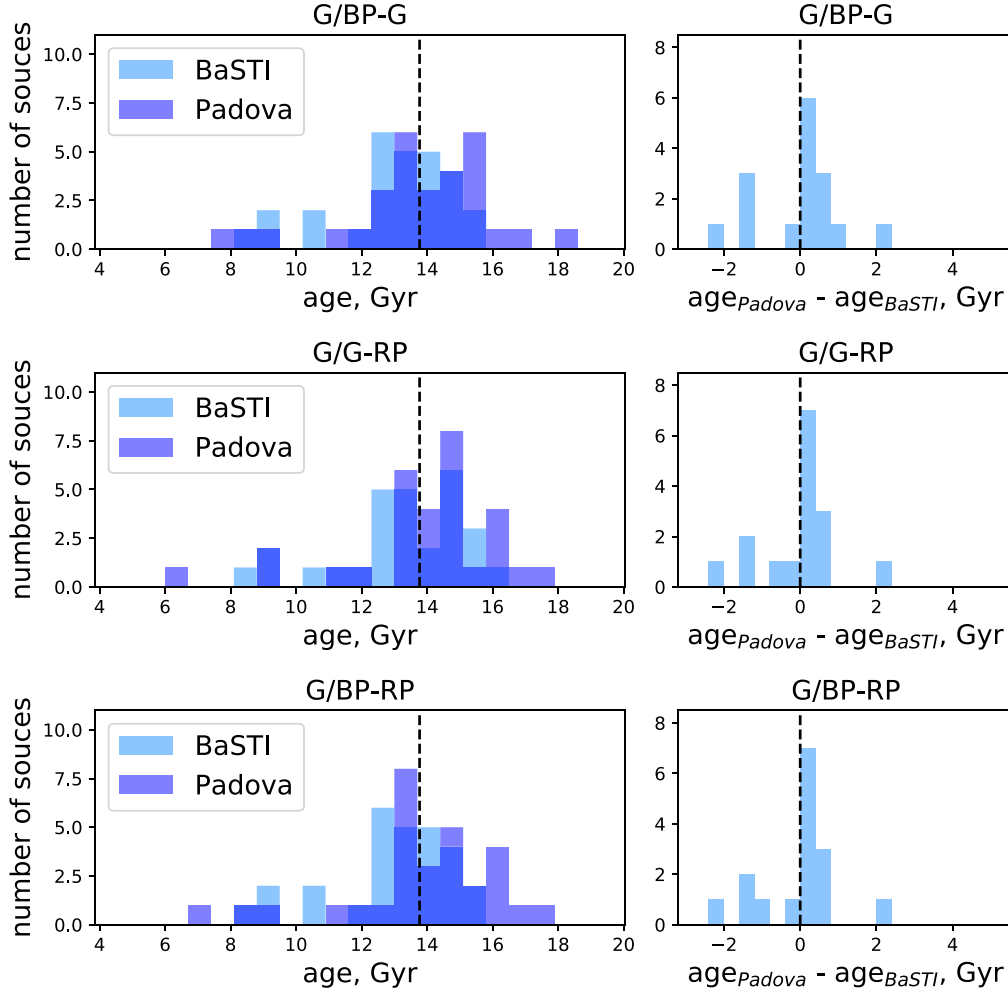
Figure 12. Left: dispersion in age determination from Padova and BaSTI isochrones in diagrams G versus $G_{BP} - G$, G versus $G - G_{RP}$, and G versus $G_{BP} - G_{RP}$. The vertical dotted line is the age of the universe, 13.77 Gyr (Bennett et al. 2013). Right: dispersion in age difference between Padova and BaSTI isochrones in diagrams G versus $G_{BP} - G$, G versus $G - G_{RP}$, G versus $G_{BP} - G_{RP}$. The vertical dotted line is a zero-point.

within the errors. This means that ages derived with different filter combinations are the same.

8.2. Comparison with Old Metal-poor Globular Clusters: M30, M92, and NGC 6397

We used metal-poor globular clusters (GCs) as a test of our age determination technique. We calculated the age for each star the GCs located in the turnoff-point region ($2.4 < G < 4.7$ mag). All parameters for age determination of GCs are listed in

Table 7. Parallax was derived as a mean parallax from Gaia DR3 of all members of the cluster. All three GCs are located far from the Sun (>2.5 kpc). They lie outside the Green et al. (2018) reddening map and are far from the edge of the Lallement et al. (2018) reddening map; that is why we choose extinction coefficients from the 2D Schlegel et al. (1998) map. Metallicities are taken as an average of results listed in the SIMBAD catalog.[8]

---

[8] http://simbad.u-strasbg.fr/simbad/sim-fbasic
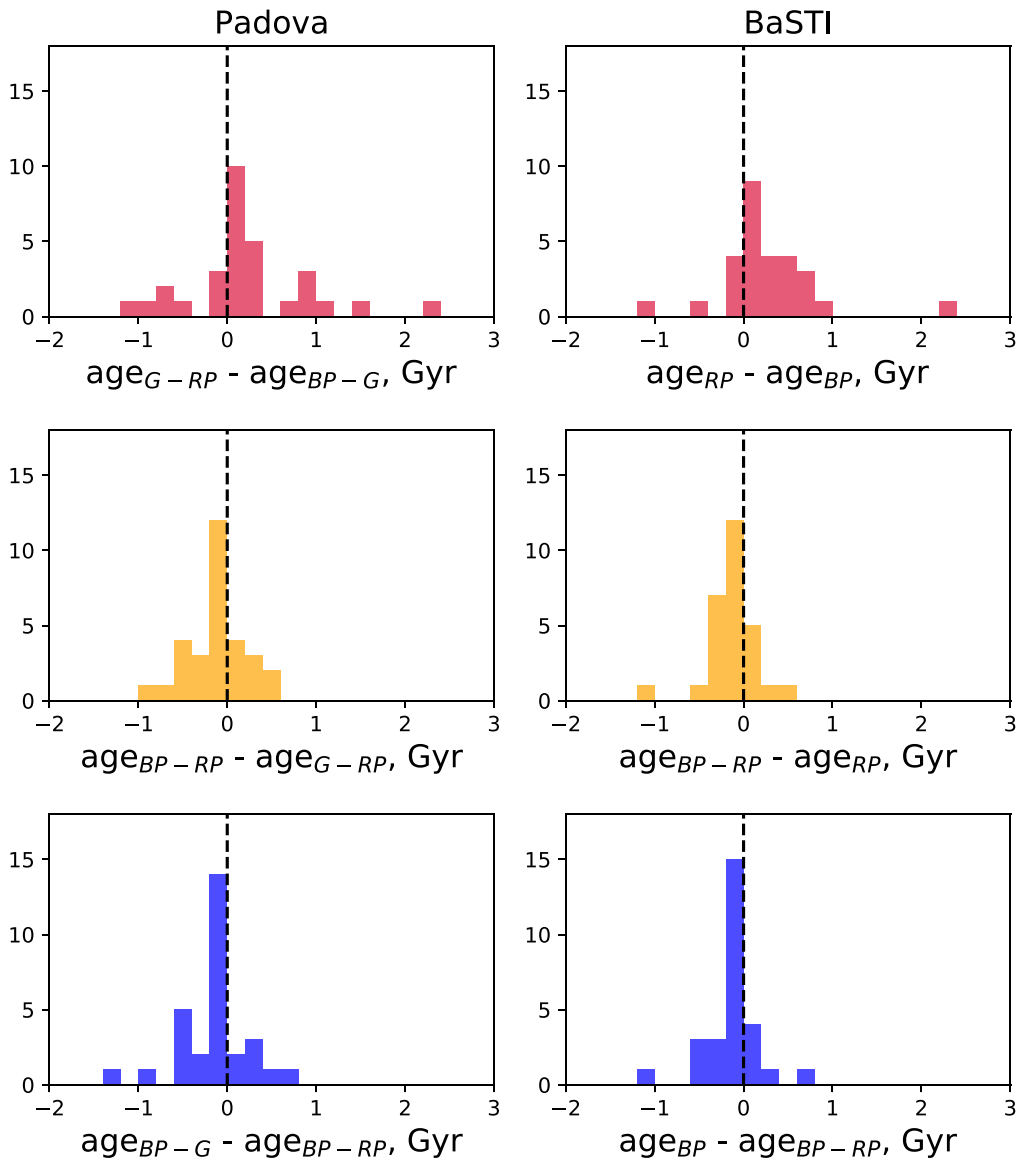
Figure 13. Dispersion of differences in age from different filter combinations: G versus $G_{BP} - G$, G versus $G - G_{RP}$, and G versus $G_{BP} - G_{RP}$ for Padova and BaSTI isochrones. The vertical dotted line is at zero.

Reference ages were collected from Correnti et al. (2018; NGC 6397), Kains et al. (2013; M30), and VandenBerg et al. (2016; M92).

First, we checked the accuracy of our automatic age determination method by comparing the age derived by different authors with our results. As we can notice in Figure 14, the age determined by our method is in a good agreement with ages derived by other authors. Only for M30 is our age slightly younger. This inconsistency is caused by uncertainties of the input data, especially in parallax and reddening.

Second, we compared the distribution of the ages of the GCs with the age distribution of metal-poor stars. In Figure 14, we can see that on average our metal-poor stars are older than all three GCs by about 1 Gyr. Also, it is worth mentioning that the width of the GCs' age distribution shows that stars whose age is older than the age of the universe can be explained within the natural dispersion of the parameters in the same way as in GCs.

Table 7
Globular Cluster Parameters

Name	[Fe/H] dex	Age Gyr	π mas	d pc	A_V mag	Age (ref.) Gyr
NGC 6397	−1.99	12.9	0.397	2519	0.614	12.6
M30	−2.3	12.1	0.117	8547	0.170	13.0
M92	−2.3	12.6	0.108	9259	0.072	12.5

8.3. Comparison with the Three Ancient Stars HD 84937, HD 132475, and HD 140283

We made an additional sanity check by comparing our results with the three very old stars HD 84937, HD 132475, and HD 140283. They were studied by VandenBerg et al. (2014). HD 140283 was studied also by Bond et al. (2013). Both studies discovered that these stars are old and close to the age of the universe. We used our age determination technique to derive their age. We used photometry and parallaxes from
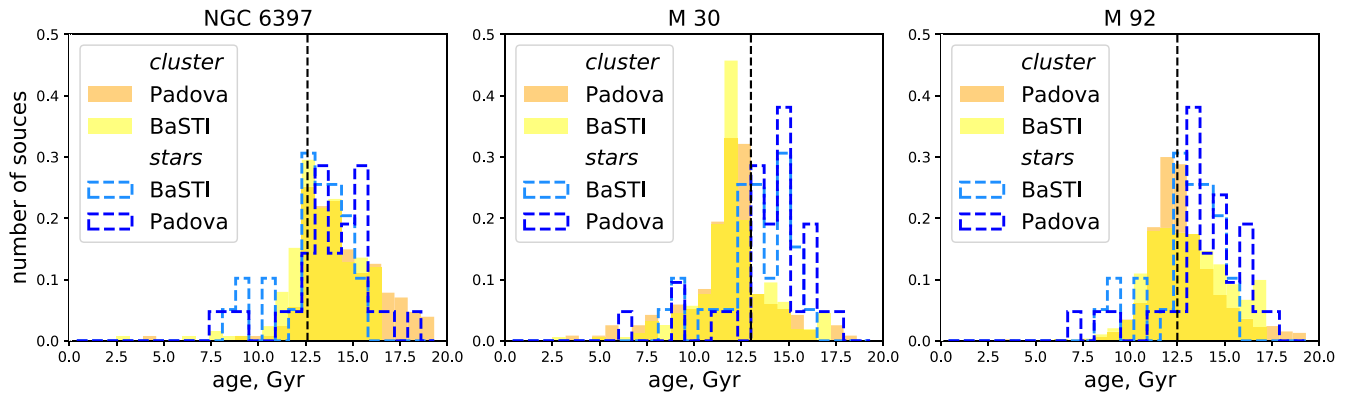
Figure 14. Dispersion of ages for GCs NGC 6397, M30, and M92 compared with metal-poor stars under investigation.

Gaia DR3, metallicity from the SIMBAD catalog,[9] and reddening from Lallement et al. ([2018]). All parameters are listed in Table [8]. The resulting ages are shown in the Table [9]. We can see that our results are close to the previously derived ages and they coincide within the uncertainties.

8.4. Age Averaging

Finally, we calculated the arithmetic and weighted average age for all the stars (Table [10]). The average age is very close to the age of the universe, which means that most of the stars under consideration were born recently after the Big Bang. The provided uncertainties take into account only the formal internal errors. But, obviously, we may have additional error sources coming, for example, from isochrone models: convection treatment, element diffusion (the settlement of heavy elements and consequent incorrect global metallicity derived from the actual stellar atmosphere; Bonfanti et al. [2015]) and temperature–color transformations. There are also subtle effects due to the overabundance of oxygen on the "shape" of the turnoff-point (VandenBerg et al. [2014]) and the impact on opacity from C, Ca, and Mg (Section [6.1]). Another important external error could be the gas/dust ratio implied in the reddening derivation of the Lallement et al. ([2018]) map based on gas. We may reasonably suppose that they account for about 0.5 Gyr (this corresponds to an A_V error of ± 0.05 mag at the main-sequence turnoff). The comparison between the two different sets of isochrones we use and our age determination of the three reference globular clusters suggest that 0.5 Gyr is a good estimation for our systematic error.

8.5. Age–Metallicity Relation

The age–metallicity relation (AMR) from G versus $G_{BP} - G$, G versus $G - G_{RP}$, and G versus $G_{BP} - G_{RP}$ diagrams is presented in Figure [15] and, for the average age, in Figure [16], together with three ancient stars from VandenBerg et al. ([2014]) and three metal-poor GCs: NGC 6397, M30, and M92. The first column shows results from the Padova isochrones, and the second column is from BaSTI. For the comparison, we took the Milky Way globular cluster AMR from Dotter et al. ([2011]; their Figure 10) and Cohen et al. ([2021]; their Figure 4), which are shown as dashed lines in Figures [15] and [16]. We can see that our stars extend the AMR to the lower metallicity side. On average, the metal-poor stars under investigation are older by about 0.8 Gyr than the main trends of literature samples. And it
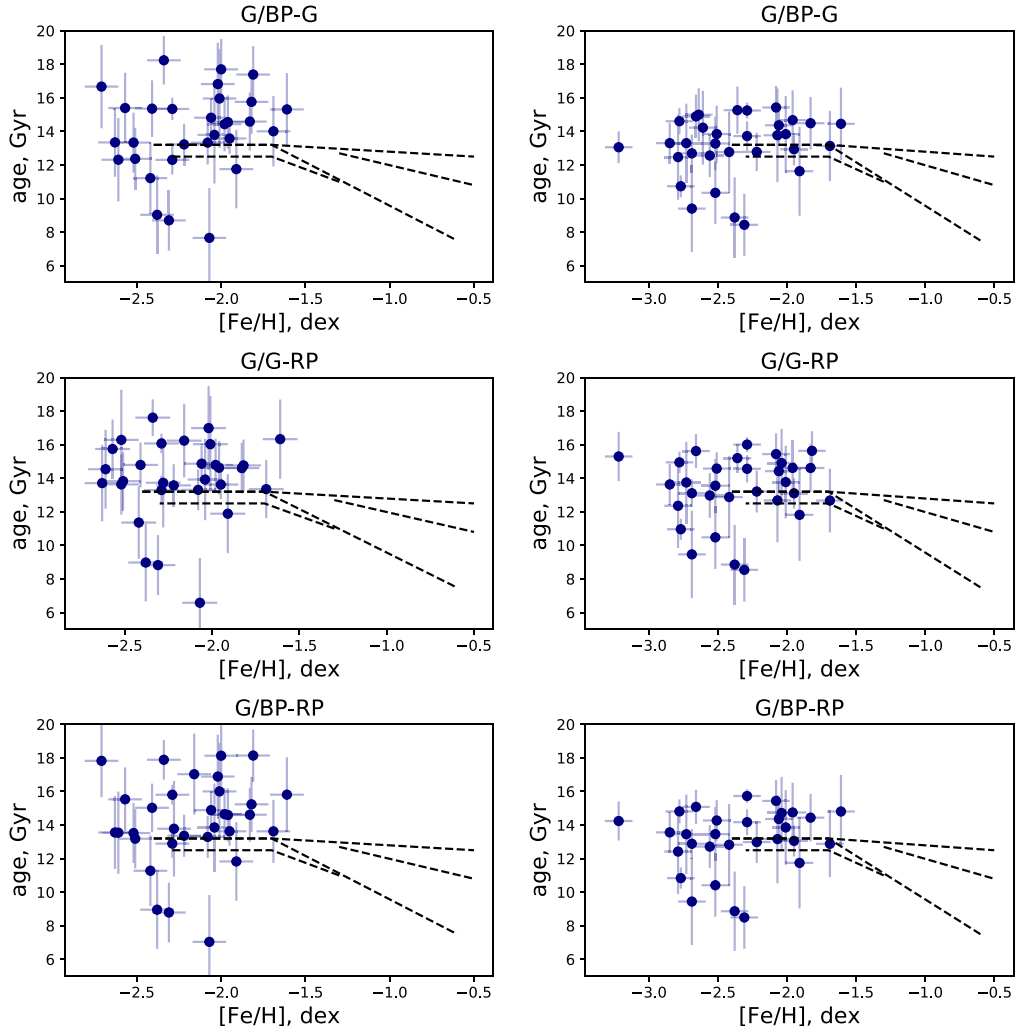
Table 8
VandenBerg et al. ([2014]) Star Parameters

Parameter	HD 84937	HD 132475	HD 140283
G, mag	8.207	8.391	7.036
G_{BP}, mag	8.423	8.692	7.321
G_{RP}, mag	7.817	7.898	6.562
π, mas	13.498	10.671	16.267
$\Delta\pi$, mas	0.044	0.025	0.026
[Fe/H], dex	-2.0	-1.4	-2.4
[α/Fe], dex	0.38	0.45	0.26
A_V, mag	0.009	0.047	0.006
ΔA_V, mag	0.047	0.056	0.053

Table 9
Age Derived for VandenBerg et al. ([2014]) Stars

Star	Source	BaSTI Age	BaSTI Error	Padova Age	Padova Error
HD 84937	G versus $G_{BP} - G$	13.18	± 1.40	12.03	± 1.41
	G versus $G - G_{RP}$	14.8	± 1.05	13.96	± 1.31
	G versus $G_{BP} - G_{RP}$	14.21	± 1.28	13.1	± 1.22
	average	14.06	± 1.51	13.03	± 1.79
	VandenBerg et al. ([2014])	12.08	± 0.14		
HD 132475	G versus $G_{BP} - G$	13.28	± 1.27	13.16	± 1.14
	G versus $G - G_{RP}$	14.16	± 1.27	14.09	± 1.32
	G versus $G_{BP} - G_{RP}$	13.68	± 1.14	13.64	± 1.18
	average	13.71	± 0.81	13.63	± 0.86
	VandenBerg et al. ([2014])	12.56	± 0.46		
HD 140283	G versus $G_{BP} - G$	14.02	± 1.27	14.13	± 1.3
	G versus $G - G_{RP}$	14.7	± 1.17	15.24	± 1.56
	G versus $G_{BP} - G_{RP}$	14.51	± 1.29	14.71	± 1.44
	average	14.41	± 0.65	14.69	± 1.03
	VandenBerg et al. ([2014])	14.27	± 0.38		
	Bond et al. ([2013])	14.46	± 0.31		

is consistent with our results in Section [8.2], where we showed that GCs on average show younger ages compared with single metal-poor stars. The average age for the data set under consideration is 13.7 ± 0.4 Gyr (BaSTI, 28 stars), 13.9 ± 0.5 Gyr (Padova, 17), and 14.1 ± 0.3 Gyr (from BaSTI and Padova, 17

Figure 15. Age–metallicity relation for ages from G versus $G_{BP} - G$, G versus $G - G_{RP}$, and G versus $G_{BP} - G_{RP}$ diagrams. First column: ages are from Padova isochrones; second column: from BaSTI.

Table 10
Average Ages of Our Stars

Isochrone	Filter	Average age Gyr	Error Gyr	Weighted average age Gyr	Error Gyr
Padova	G versus $G_{BP} - G$	13.6	±1.3	13.7	±1.1
	G versus $G - G_{RP}$	13.9	±1.4	14.1	±1.2
	G versus $G_{BP} - G_{RP}$	13.8	±1.3	13.9	±1.1
	average	13.7	±0.5	13.9	±0.5
BaSTI	G versus $G_{BP} - G$	13.4	±0.7	13.5	±0.7
	G versus $G - G_{RP}$	13.6	±0.7	13.9	±0.7
	G versus $G_{BP} - G_{RP}$	13.5	±0.8	13.7	±0.7
	average	13.5	±0.4	13.7	±0.4
Padova+BaSTI	average	13.8	±0.3	14.1	±0.3

stars). Moreover, for metallicity between −2.7 and −2.0 dex, we have a minor population with relatively younger ages of around 8–10 Gyr. It can be an indication of two different populations or two epochs of star formation.

9. Conclusion

In this study, we derived the ages of 28 metal-poor stars (Table 6). The average age from Padova isochrones is 13.9 ± 0.5 Gyr,

from BaSTI 13.7 ± 0.4 Gyr, and for stars with both determinations, it is 14.1 ± 0.3 Gyr (internal errors only). Our estimate for the additional systematic error is around 0.5 Gyr.

Ages were derived by automatic isochrone CMD fitting using Gaia DR3 photometry and the most updated parameters for distance and reddening. We considered also B,V photometry. Distances were chosen from among four sources: Gaia DR3 (Gaia Collaboration 2021), Gaia DR3 corrected by
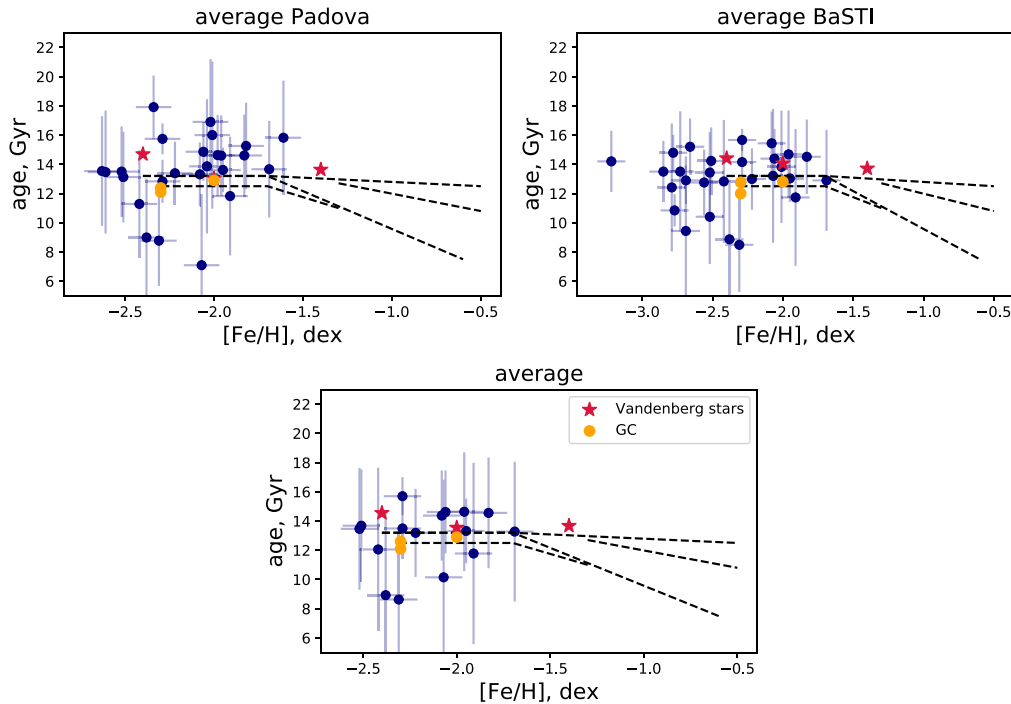
Figure 16. Average age–metallicity relation for Padova (top left), BaSTI (top right) and Padova+BASTI averaged together (bottom). Red stars are VandenBerg et al. (2014) targets. Yellow dots are three GCs: NGC 6397, M30, and M92.

Lindegren et al. (2021), Bailer-Jones et al. (2021), and Queiroz et al. (2020; StarHorse). Gaia DR3 parallaxes showed the best results in terms of CMD dispersion. We ascribe this result to the relative brightness of our stars. The best reddening estimate was obtained by combining two reddening maps: Green et al. (2018) and Lallement et al. (2018) extended by Montalto et al. (2021).

We used two sets of isochrones, Padova and BaSTI. Padova isochrones produce on average 0.5 Gyr older ages than BaSTI isochrones. Age determination can depend also on the detailed chemical composition of the stars. The enhancement of α-elements, C, N, O, and Ne can significantly affect the opacity of metal-poor stars and change the continuum emission. The strongest effect is in the Johnson B filter (Figure 8). The effect is marginally present also in Gaia filters, but, due to their width, it is much less prominent. We suggest that, in order to improve the age determination, specific isochrones should be computed for the chemical composition of each star.

In order to minimize the chemical composition effect in this work we used three different filter combinations of Gaia filters: G versus $G_{BP} - G$, G versus $G - G_{RP}$, and G versus $G_{BP} - G_{RP}$. We found that the age difference from one combination to the other is about 0.2 Gyr or less, smaller than the total uncertainty of the age determination method (more than 0.5 Gyr).

We checked our results against the three most metal-poor GCs: NGC 6397, M30, and M92. The GC ages derived by our automatic isochrone-fitting technique are in good agreement with ages derived by other authors (Correnti et al. 2018 for NGC 6397, Kains et al. 2013 for M30, and VandenBerg et al. 2016 for M92). Moreover, our set of very metal-poor stars on average is older than the most metal-poor GC by about 1 Gyr.

Additionally, we compared our results with the ages of three nearby ancient halo subgiants (VandenBerg et al. 2014). We found that our ages coincide within the uncertainties with the VandenBerg et al. (2014) and Bond et al. (2013) ages. The results are summarized in Table 9.

Finally, we studied the age–metallicity relation in its very metal-poor tail. The trend is almost horizontal, but our stars are on average older than the mean locus found by other authors (Dotter et al. 2011; Cohen et al. 2021) by about 0.8 Gyr. The interesting fact is that we found a group of very metal-poor stars with significantly younger ages of 8–10 Gyr. The ages of these stars can be a signature of two different populations or two epochs of star formation.

Our future plans include:

1. Extending our data set to the newly available samples of metal-poor and very metal-poor stars (Li et al. 2022; Lucey et al. 2022; Xu et al. 2022)
2. Assessing the origin of these stars through the detailed analysis of their kinematics and chemical composition.

ORCID iDs

Anastasiia Plotnikova https://orcid.org/0000-0002-7504-0950
Giovanni Carraro https://orcid.org/0000-0002-0155-9434
Sandro Villanova https://orcid.org/0000-0001-6205-1493
Sergio Ortolani https://orcid.org/0000-0001-7939-5348

References

Ade, P. A. R., Aghanim, N., Armitage-Caplan, C., et al. 2014, A&A, 571, A16
Bailer-Jones, C. A. L., Rybizki, J., Fouesneau, M., Demleitner, M., & Andrae, R. 2021, AJ, 161, 147
Barklem, P. S., Christlieb, N., Beers, T. C., et al. 2005, A&A, 439, 129
Bennett, C. L., Larson, D., Weiland, J. L., et al. 2013, ApJS, 208, 20
Bird, J. C., Kazantzidis, S., & Weinberg, D. H. 2012, MNRAS, 420, 913
Bonaca, A., Conroy, C., Cargile, P. A., et al. 2020, ApJL, 897, L18
Bond, H. E., Nelan, E. P., VandenBerg, D. A., Schaefer, G. H., & Harmer, D. 2013, ApJL, 765, L12
Bonfanti, A., Ortolani, S., Piotto, G., & Nascimbeni, V. 2015, A&A, 575 A18
Bromm, V., & Larson, R. B. 2004, ARA&A, 42, 79
Carter, C., Conroy, C., Zaritsky, D., et al. 2021, ApJ, 908, 208
Cayrel, R., Depagne, E., Spite, M., et al. 2004, A&A, 416, 1117
Christlieb, N., Beers, T. C., Barklem, P. S., et al. 2004, A&A, 428, 1027
Cohen, R. E., Bellini, A., Casagrande, L., et al. 2021, AJ, 162, 228
Correnti, M., Gennaro, M., Kalirai, J. S., Cohen, R. E., & Brown, T. M. 2018, ApJ, 864, 147
Dotter, A., Sarajedini, A., & Anderson, J. 2011, ApJ, 738, 74
El-Badry, K., Rix, H.-W., & Heintz, T. M. 2021, MNRAS, 506, 2269
Feuillet, D. K., Bovy, J., Holtzman, J., et al. 2018, MNRAS, 477, 2326
Frebel, A., & Norris, J. E. 2015, ARA&A, 53, 631
Gaia Collaboration 2021, A&A, 649, A1
Gaia Collaboration, De Ridder, J., Ripepi, V., et al. 2022, arXiv:2206.06075
Green, G. M., Schlafly, E. F., Finkbeiner, D., et al. 2018, MNRAS, 478 651

Grenon, M. 1972, in IAU Coll. 17: Age des Etoiles, ed. G. Cayrel de Strobel & A. M. Delplace (Cambridge: Cambridge Univ. Press), 55
Grenon, M. 1989, Ap&SS, 156, 29
Hidalgo, S. L., Pietrinferni, A., Cassisi, S., et al. 2018, ApJ, 856, 125
Kains, N., Bramich, D. M., Arellano Ferro, A., et al. 2013, A&A, 555, A36
Lallement, R., Capitanio, L., Ruiz-Dern, L., et al. 2018, A&A, 616, A132
Li, H., Aoki, W., Matsuno, T., et al. 2022, ApJ, 931, 147
Limberg, G., Santucci, R. M., Rossi, S., et al. 2021, ApJ, 913, 11
Lindegren, L., Bastian, U., Biermann, M., et al. 2021, A&A, 649, A4
Lucey, M., Al Kharusi, N., Hawkins, K., et al. 2022, arXiv:2206.08299
Montalto, M., Piotto, G., Marrese, P. M., et al. 2021, A&A, 653, A98
Queiroz, A. B. A., Anders, F., Chiappini, C., et al. 2020, A&A, 638, A76
Quillen, A. C., Minchev, I., Bland-Hawthorn, J., & Haywood, M. 2009, MNRAS, 397, 1599
Ritter, J. S., Safranek-Shrader, C., Gnat, O., Milosavljević, M., & Bromm, V. 2012, ApJ, 761, 56
Roškar, R., Debattista, V. P., Stinson, G. S., et al. 2008, ApJL, 675, L65
Safranek-Shrader, C., Milosavljevic, M., & Bromm, V. 2014, MNRAS, 440, L76
Salaris, M., Chieffi, A., & Straniero, O. 1993, ApJ, 414, 580
Schlafly, E. F., & Finkbeiner, D. P. 2011, ApJ, 737, 103
Schlaufman, K. C., & Casey, A. R. 2014, ApJ, 797, 13
Schlegel, D. J., Finkbeiner, D. P., & Davis, M. 1998, ApJ, 500, 525
Sellwood, J. A., & Binney, J. J. 2002, MNRAS, 336, 785
Twarog, B. A. 1980, ApJ, 242, 242
VandenBerg, D. A., Bond, H. E., Nelan, E. P., et al. 2014, ApJ, 792, 110
VandenBerg, D. A., Denissenkov, P. A., & Catelan, M. 2016, ApJ, 827, 2
Xu, S., Yuan, H., Zhang, R., et al. 2022, arXiv:2207.02371